U.S. Department of Energy Collegiate Wind Competition: Technical Design Report 2019

Prepared By:

Bear, Nicholas

Graham, Adam

Ito, Devyn

Kizilkaya, David

Logier, Reagan

Rodriguez, Samuel

Sadamune, Alexander

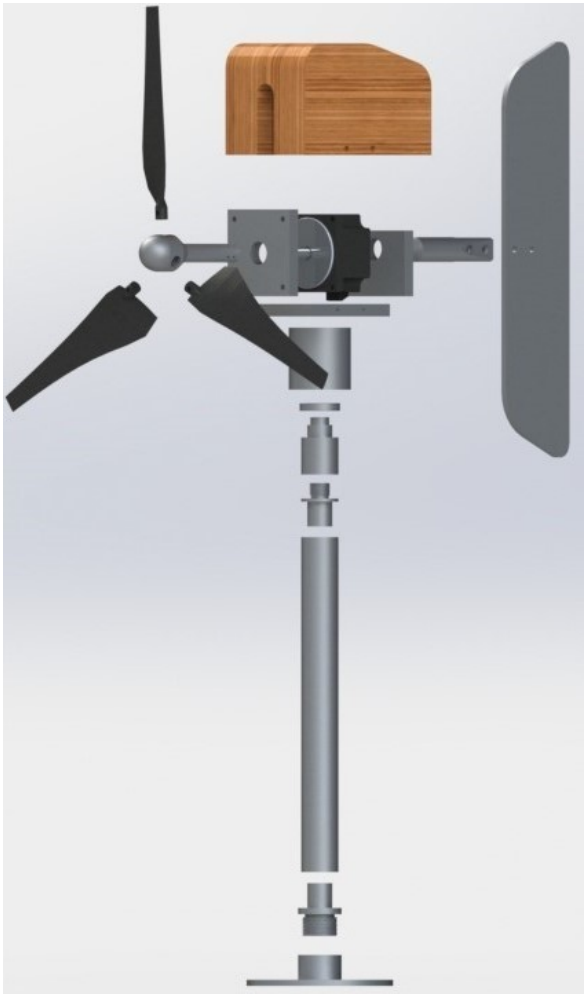

Project Advisors: Dr. Tom Nordenholz, Dr. Evan Chang-Siu, Randy Thomas, Steffan Long

CSU - Maritime Academy

April 21st, 2019

Table of Contents

Chapter 1: Executive Summary

Our team's objective this year was to build off the previous year's design and improve its performance, specifically start-up. We improved the overall documentation of the design, build, and analysis process as well. In previous years, their research was not well documented. This forced the following team to repeat research that had already been conducted. To improve documentation, we conducted multiple trade-off studies to validate design decisions, and worked closer with underclassmen to make the transition between teams an easier process. For this competition, we designed a fixed-pitch, three-blade, stall-controlled, passive yaw, small-scale wind turbine. Our shaft drives a synchronous brushless DC generator that produces three-phase AC power.

For our wind turbine, a brushless DC generator is used to convert mechanical energy into electrical power. Said brushless DC generator was selected after extensive research. Throughout the research process, over fifteen generators were benchmarked using a generator selection matrix which compared theoretical performance of generators at typical competition operating conditions. Once the generator was selected, it was purchased and tested to validate the provided technical specifications. Using measured generator performance characteristics, a theoretical system performance model was created that allowed us to observe system performance relative to wind power curves.

During start-up, the turbine is run as a motor by exciting the three phases using a DC-AC inverter which allowed us to overcome the initial start-up torque at a lower wind-speed. Through testing, we were able to determine an appropriate time to switch from running the turbine as a motor to a generator. Once power is generated, the three-phase AC is converted into DC power using a full-bridge rectifier. The output from the rectifier is fed into a buck-boost converter. The buck-boost converter influences the rotor speed which allowed us to control the power output. In addition, we selected a 6V lead-acid battery as our load and the objective of the system is to charge this battery. A benefit of this load selection is that it is possible to pull current from the battery to power our controls when the turbine is not running.

Controls for the turbine electronics were implemented via Arduino MEGA2560 microcontrollers, with a priority on safety and reliability. Separate codes were written for the Main Task and the Durability Task with control constants determined through experimentation. Numerical modeling was also done via transient simulations of the buck-boost converter in LTspice. This model provided a theoretical basis from which to select new electrical components for prototyping different boards.

The design of the blades consists of two airfoils: the SD-7080 and the SD-8064. The SD-7080 was chosen for its power performance at low Reynolds Numbers. The SD-8064 was selected for its larger thickness to chord ratio which provided structural support for the blade. An iterative process involving QBlade analysis, manufacturing, and testing was used to complete the design of the blades.

Chapter 2: Blade Design

2.1 Blade Analysis

The blades are comprised of two airfoils: the SD-7080 and the SD-8064 [5]. These two specific airfoils were chosen not only because of their characteristics, but also because they have a similar optimal angle of attack which provided a smoother transition from one airfoil to another. The SD-7080 airfoil is a thinner airfoil with a thickness to chord ratio of 9.2%. The purpose of this airfoil is to produce as much power as possible. It is important for this airfoil to have a smaller thickness to chord ratio because it results in better performance at low Reynolds Numbers. The SD-8064 airfoil is a thicker airfoil with a thickness to chord ratio of 12.3%. This airfoil will not produce as much power but provides greater structural support for the blade.

2.1.1 QBlade

QBlade is an open source software that utilizes XFOIL and BEM theory, which was used to conduct the theoretical analysis and design of the blades [6]. To properly use QBlade, the Reynolds Number had to be known. This is an important assumption that had to be made, and after an iterative process, it was determined that the approximate Reynolds Number was 50,000. The Reynolds Number changes a little depending on the position of the blade, especially at the root; but for the most part 50,000 is fairly constant along the blade. Using this as the Reynolds Number, QBlade was able create a plot that showed the coefficient of lift over the coefficient of drag vs. the angle of attack. Using this plot, a design angle of attack was found. By knowing the angle of attack and choosing a design tip speed ratio (TSR), which is the ratio of the speed of the tip of the bade over the speed of the wind, Schmitz optimization was used to create the geometry of the blade.

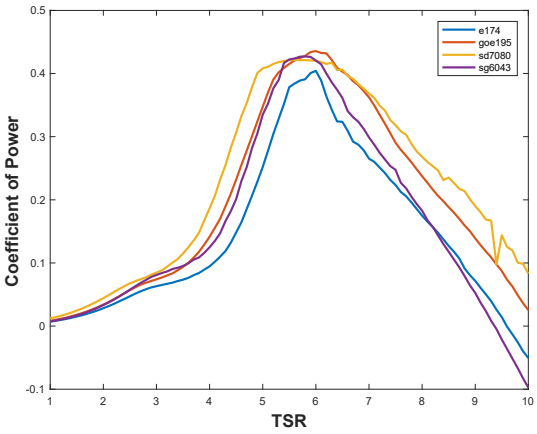

Figure 2.1: Airfoil comparison of power performance

The Schmitz optimization finds the optimized chord and pitch angle at each radial position along the blade to produce the most power for a given design TSR and angle of attack (Equations 2.1 and 2.2). This optimization accounts for wake rotation but ignores drag and tip loss. It utilizes the following equations to find the chord, c, and pitch angle, θ_p [3].

$$\varphi = \frac{2}{3}\tan^{-1}\left(\frac{1}{\lambda_r}\right) \qquad \text{Equation 2.1}$$

$$c = \frac{8\pi r}{BC_l}(1-\cos\varphi) \qquad \text{Equation 2.2}$$

$$\theta_p = \varphi - \alpha \qquad \text{Equation 2.3}$$

Here, φ is the angle of the relative wind, λ_r is the local TSR, c is the chord, r is the radius, B is the number of blades, C_l is the coefficient of lift, and α is the angle of attack.

Once the blade geometry had been optimized, QBlade was used to calculate two plots, the coefficient of power vs. TSR, and the start-up torque vs. wind speed. The first plot shows the non-dimensional power that is being produced by the rotor, and the second plot shows start-up torque at a rotor speed of 0. By comparing this with the cogging torque of the generator, the cut-in wind speed was determined. Using these plots, an iterative process using many different airfoils was completed. This analysis can be seen in Figure 2.1 and Figure 2.2. After the analysis was completed, it was decided that the SD-7080 would be the best airfoil because of its high coefficient of power, the fact that it is flat at the peak allowing for easier control, and the higher starting torque.

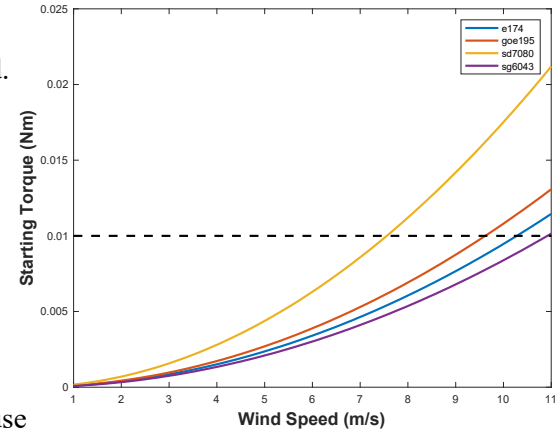

Figure 2.2: Airfoil comparison of starting torque

The base airfoil that provides the structural support for the blade was chosen to be the SD-8064. It was chosen for its larger thickness to chord ratio. This is desirable because it results in better structural integrity. The SD-8064 also has a similar design angle of attack as the SD-7080, which makes the transition from one blade to another smoother.

2.2 3-Blades Vs. 4-Blades

Using QBlade, a trade-off study was conducted between a 3-blade rotor and a 4-blade rotor design. In previous years a 3-blade rotor design has been the standard. The purpose of this study was to confirm that a 3-blade rotor was the best design choice.

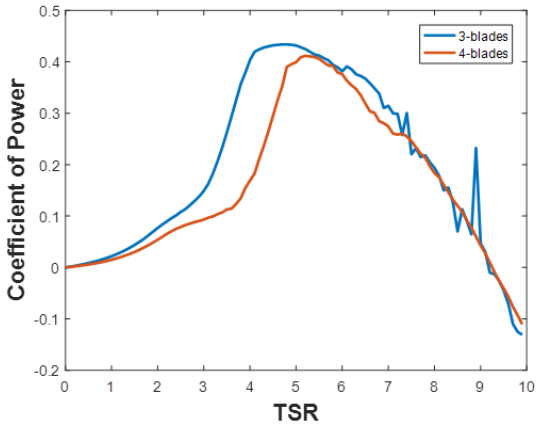

Figure 2.3: 3 and 4-blade design comparison of power performance

To do this study, an iterative process was used to find the best 3-blade design and compare it to the best possible 4-blade design. Both the blade designs utilized the same airfoils, the SD-7080 and the SD-8064. To decide the best design, the previously mentioned plots were analyzed.

As can be seen in Figure 2.3, and Figure 2.4, the 4-blade rotor design performed worse in both power production and cut-in wind speed. Looking back on the Schmitz Optimization, the equation to find the chord is inversely proportional to the number of blades. By increasing the number of blades, the chord

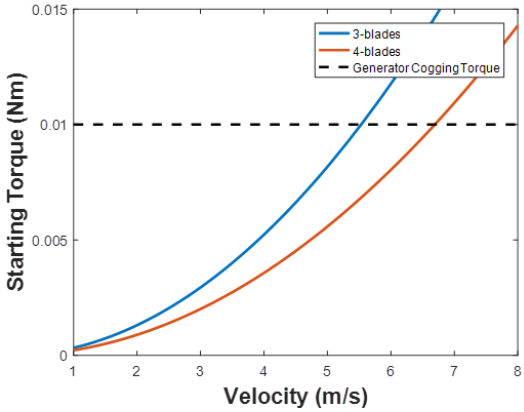

Figure 2.4: 3 and 4 blade design comparison of starting torque

decreases (Equation 3.2), which results in a lower Reynolds Number. With a lower Reynolds Number, the perfomance of the blade drops. This anlaysis helped confirm that a 3-blade design was the best choice for our design.

2.3 Blade Design and Testing

A QBlade analysis can only go so far, so once the airfoils were chosen, an iterative process was used to test the blades in our wind tunnel. The design angle of attack and the design TSR were varied and the result were recorded in Table 2.1. Using both the rated power output at 11m/s, and the cut-in wind speed, the blade designs were compared.

Blade Design			Test Results	
TSR	Angle of Attack	Number of Blades	Power (W)	Cut-in wind speed (m/s)
4.5	5.5	3	45	6.3
5.5	6	3	43	9
5	6	3	40	7.8
5	5.5	3	47	6.2

Table 2.1: Experimental comparison of blade performance

2.4 Final Blade Design and Manufacturing

The blade design we decided to go with is highlighted in Table 2.1. This blade was chosen because of the high-power output and low cut-in wind speed, which is shown in Figure 2.3 and Figure 2.4. This blade design can be seen in Table 2.2.

The blades were 3-D printed on a MakerBot Replicator+, using PLA with 100% infill. The blades were orientated lengthwise so that the layers of the PLA filament went along the blade. Once the blades were printed, they were gently sanded to remove any impurities.

Position	Chord	Twist	Airfoil
m	m	Deg	
0.01905	0.05318	42	SD-8064
0.039645	0.05961	28.91	Blend
0.06024	0.05238	20.01	Blend
0.080835	0.004431	13.9	Blend
0.10143	0.03769	10.45	SD-7080
0.122025	0.03252	8	SD-7080
0.14262	0.02848	6.17	SD-7080
0.163215	0.02527	4.78	SD-7080
0.18381	0.002268	3.67	SD-7080
0.204405	0.02055	2.78	SD-7080
0.225	0.01878	2.04	SD-7080

Table 2.2: Blade geometry for final design

2.5 Blade Loading

An important analysis for the blades was the load analysis. This analysis finds the stress and deflection of the blades based on the forces the blade experiences. These forces include the flapwise aerodynamic loading, which was obtained from QBlade, and the centrifugal forces which were calculated separately using the rotational speed, blade geometry, and the material used.

The first part of the analysis is the stress analysis. This analysis was used to find the bending and axial stress at the worst operating conditions. Two conditions were analyzed: a wind speed of 11m/s and a

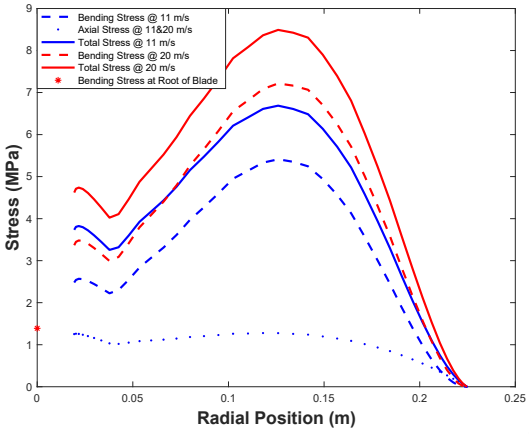

Figure 2.5: Total stress of blade at a wind speed of 11 and 20 m/s

rotor speed of 3000rpm, and a wind speed of 20m/s and a rotor speed of 3000rpm. During the QBlade analysis, the rotor was seen to have a theoretical speed of about 2200rpm, but through experimental data it was determined that the actual rotor speed reached 3000rpm. To complete this analysis, we needed the area and the moment of inertia of the blades. Since, the blades are not a simple geometric shape, finding these values was complicated. These values we found by using approximating equations [4]. Once the area and moment of inertia were known, an integration was used to find the bending and axial stresses. These stresses can be seen in Figure 2.5. The bending stress at the blade root due to the force of the wind was also calculated. The root is subject to a bending stress of 1.39MPa at a wind speed of 20m/s and 3000rpm. This point can be seen on Figure 2.5. This resulted in a safety factor of 12.4.

This analysis provided the max stress the blade experiences, which through an iterative process of testing in a wind tunnel, was found to be at the rated wind speed of 20m/s and a rotational speed of 3000 rpm. The blade experienced a max stress of 8.5MPa under those conditions. The blades were 3-D printed using PLA which has a density of 1.25g/cm^3, a Young's modulus of 2.1GPa, and a yield strength of 34.5MPa. This data was acquired through tensile tests on a universal testing machine in our materials lab. The safety factors for the two conditions are 5.3 and 4.1 for a wind speed of 11m/s and 20m/s respectively. This assured that the blades were sufficient to withstand the stresses inflicted by the wind.

The other analysis that had to be conducted was the deflection analysis. This analysis utilizes the Euler-Bernoulli beam theory, which fails to take into account the centrifugal force that will help straighten out the blade. The data can be seen in Figure 2.6. The deflection of the blade was calculated at 20m/s which is the wind speed that would deflect the blade the most. At this wind speed, a deflection of about 6.5cm is seen.

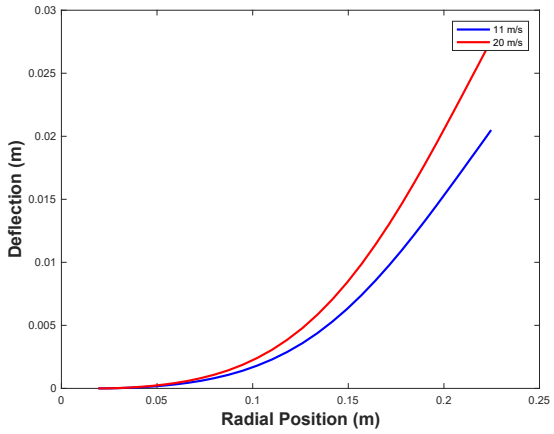

Figure 2.6: Deflection of blade at wind speeds of 11 and 20 m/s

Chapter 3: Mechanical Design

3.1 Overview

An exploded view of the turbine can be seen on the cover of this report. We chose to design a three-blade, fixed-pitch turbine with a passive yaw system. All metallic components including the base, tower, tower inserts, generator foundation, tail root, hub and hub nose were made of 6061 aluminum. The base for the tower was manufactured on a Hass CNC mill in order to meet the dimensions specified by the competition. The tower was purchased from McMaster-Carr (OD=1.5" and ID=1") and cut down to the necessary length. The tower inserts were manufactured on a manual lathe for the purpose of connecting the base and the bearing assembly to the tower. A tolerance of 0.005" was applied to ensure a close fit between the tower and tower inserts. The tower inserts are connected to the inside of the tower with LOCTITE EA 9340 epoxy. The three generator foundation plates were manufactured on a manual mill. The nacelle is made out of walnut and was partially manufactured on a manual mill and hand-shaped using a belt sander.

3.2 Generator Selection

A large component of the wind turbine performance is dependent on generator selection. The generator is used to convert the rotational energy of the shaft to electrical energy. It was decided early in the research phase that we would be utilizing a brushless DC motor because of its high power to weight density and minimal losses. For our design, we were most concerned with the voltage constant, the armature resistance, and the cogging torque of the motor. The voltage constant of the generator (commonly referred to as K_V) is the ratio of the generator's rotational speed (rpm) to the rectified DC voltage (V). The equation for induced voltage can be seen below:

$$K_V = \frac{V}{rpm} \qquad \text{Equation 3.1}$$

For our design, we decided to use a 6V battery as a load. Because of this, we primarily investigated generators which produce slightly more than 6V at an rpm of approximately 3000 (typical operating speed). A voltage slightly greater than the load voltage is desired to ensure effective charging of the battery.

When a generator produces power, some of the generated power is lost in the armature. This power loss is due to the resistance of the armature windings and the current flowing through said windings. The equation used to represent the power lost (P_L) in relation to armature resistance (R_A) can be seen below:

$$P_L = {I_A}^2 R_A \qquad \text{Equation 3.2}$$

Because of this relationship, it was imperative that a generator was selected with a relatively low armature resistance.

Cogging torque was also considered in the motor selection process. Cogging torque of a brushless DC motor is the torque which is due to the attraction between the permanent magnets on the rotor and the metal within the armature. At low wind speeds the torque being delivered to the rotor is low. The relationship between torque and wind speed can be observed in Figure 3.2. Due to this phenomenon, it is desirable to have low cogging torque in the generator—allowing the turbine to overcome the cogging torque and begin producing power at low wind speeds.

Considering all previously discussed parameters, over fifteen generators were benchmarked. Using a constructed generator comparison matrix (Table 3.1), generators were benchmarked using theoretical operating conditions—revealing induced voltage, armature current, and power losses at typical operating conditions. The armature current (I_A) was estimated by assuming a power output at the rectifier of 40W and dividing by the induced voltage at 3000rpm. After extensive research and testing, the generator selection converged on a Moons' Motor 100Watts Frame 80 Brushless DC Motor—which can be seen in the first row of Table 3.1.

Generator Comparison Matrix			V_{ind} @ Ω=2500 (Volts)	V_{ind} @ Ω=3000	I_A @ Ω=2500 & 40W	P_L @Ω=2500 & 40W	Price ($)
Moon Industries: 80BLD100L2			12.10	14.52	3.31	1.97	200
Voltage Constant (v/RPM)	Armature Resistance (ohms)	Cogging Torque (Nm)					
0.00484	0.18	0.0100062					
Moon Industries: 57BLB100L2			12.75	15.30	3.14	3.15	98
Voltage Constant (v/RPM)	Armature Resistance (ohms)	Cogging Torque (Nm)					
0.0051	0.32	Pending email					
LinEngineering BL24B28-06-R0			12.63	15.15	3.17	3.21	125
Voltage Constant (v/RPM)	Armature Resistance (ohms)	Cogging Torque (Nm)					
0.00505	0.32	<0.014					

Table 3.1

3.3 Turbine Drivetrain

When considering the drivetrain of our wind turbine, we essentially had two options—direct drive or gearbox. In industry, the vast majority of full-scale wind turbines utilize a gear box. Essentially, the blades of the turbine spin a shaft, which then connects to a gear box, which then is connected to the generator. This setup allows the relative slow rpm of the shaft ($\approx 15 - 20\text{rpm}$) to be converted into a higher rpm ($\approx 1800\text{rpm}$) which is necessary for the generator to effectively produce power. As seen in Figure 6.1, our turbine experiences sufficiently high shaft rpm without gearing. The addition of mechanical gearing also adds additional losses which could be detrimental to a low speed start-up. Also, if a gearbox was used for an increase in rotor speed, the torque needed to overcome the mechanical losses and cogging torque would be increased by the same ratio. More significantly, mechanical gearboxes experience a tremendous amount of stress and any defect in a single component can cause the turbine to become nonoperational. Traditionally, wind turbines which utilize a mechanical gearbox require significantly more maintenance than their direct drive counterparts. Gear boxes are used in industry to increase the shaft rpm to a desirable rpm for the generator. However, this is not necessary for our application because as seen in Figure 6.1, our turbine experiences sufficiently high rpm without a gearbox. In conclusion, a mechanical gearbox was determined to be unnecessary, resulting in our decision to go with a direct drive turbine design.

3.4 Hub Design

The final hub design (Figure 3.1) we chose differs from designs used in the past. Past teams have all chose to design a male-style hub with protrusions from the hub that the hollow roots of the blades would slip over. We decided to design a female-style hub where the solid blade roots slip inside the hub. This design was easier to machine because it did not require the use of a CNC mill. Our hub was machined entirely on a manual mill and lathe. This design also provides additional strength in the root of the blade and allows the securing screws for the blades to be entirely hidden once the nose is attached.

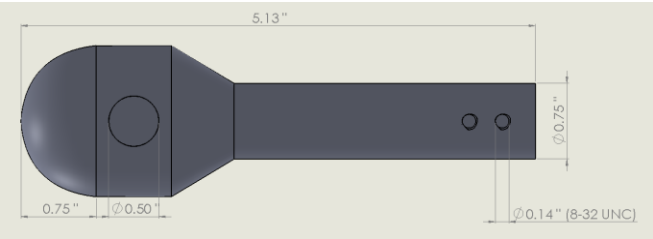

Figure 3.1: Three-blade female hub and nose cone showing basic dimensions (in).

The blades are made of PLA with a yield strength of 34.5MPa. The F_N acting on the blade root, shear stress planes, and tensile stress planes are shown in Figure 3.2**Error! Reference source not found.**. To ensure the blades would not break out of the hub, two stresses were calculated: tear out stress and tensile stress.

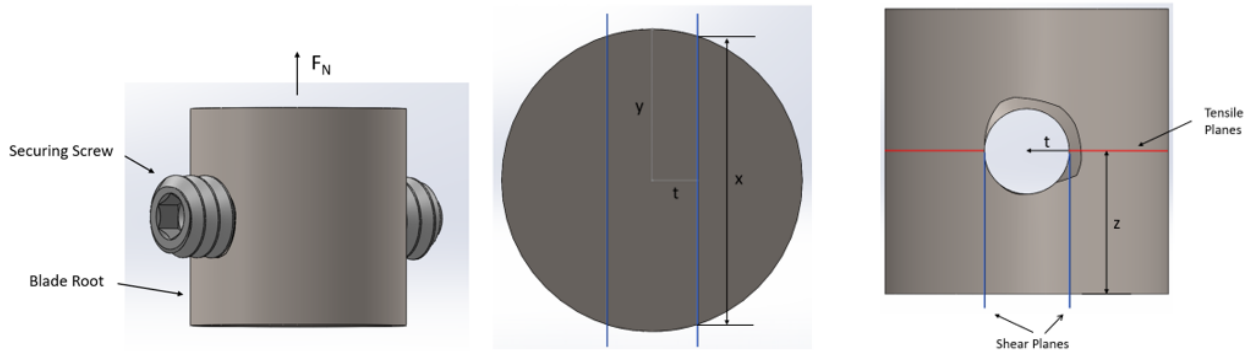

Figure 3.2: Isometric, bottom, and side view of the blade root

$$x = 2\sqrt{y^2 - t^2}$$ Equation 3.3

$$\tau = F_n/2(x * z)$$ Equation 3.4

$$\sigma_{max} = K_t \frac{4F_n}{\pi(2y)^2}$$ Equation 3.5

The centrifugal force acting on the blade root was found to be 262N at 3000rpm using the analysis described in section 3.4. The dimensions of the shear planes are given by variables x and z (Figure 3.2). Variable x was calculated using equation 3.3. [13]. The tear out stress was found to be 1.7MPa using equation 3.4. Assuming ultimate shear stress is half of ultimate tensile stress [12], this resulted in a safety factor of 10. The maximum tensile stress of 8.78MPa was calculated using equation 3.5 [11] and resulted in a safety factor of 3.9.

3.5 Tail Design

The tail rod was machined on a manual lathe and mill. It was threaded with a 1" – 8tpi tap to allow it to thread into the rear generator housing plate. It is secured on the other side of the plate by a nut. The tail is secured by two bolts running through the tail and tail rod. They are held in place by nuts on the other side.

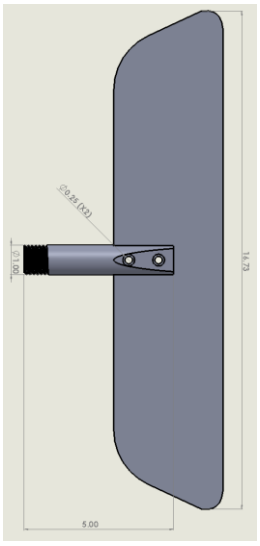

Figure 3.3: Tail assembly

3.6 Passive Yaw Bearing Assembly

The passive yaw system uses the bearing assembly (Figure 3.4) along with the wind hitting the tail to allow the turbine to rotate and correctly orient the rotor relative to the wind direction. This bearing assembly design incorporates three separate parts: the bearing housing, the bearing foundation, and an open ball bearing. The bearing housing and foundation were machined on a manual lathe. The open ball bearing has an ID=0.75", an OD=1.625" and a height of 0.3125". The bearing was press fit onto the bearing foundation using the compression force of the vice on a manual mill. An interference fit of 0.001" was used. The outer race of the bearing was then press fit into the bearing housing using the tail stock of a manual lathe. An interference fit of 0.001" was again used. The upper and lower surfaces of the bearing are pressed up against a lip 0.125" thick to allow the bearing to support the weight of the generator, nacelle, etc. The bearing foundation was threaded with a 1/2" NPT

pipe tap to allow the upper tower insert to be attached. The bearing housing is secured to the bottom generator housing plate by ¼-24 screws.

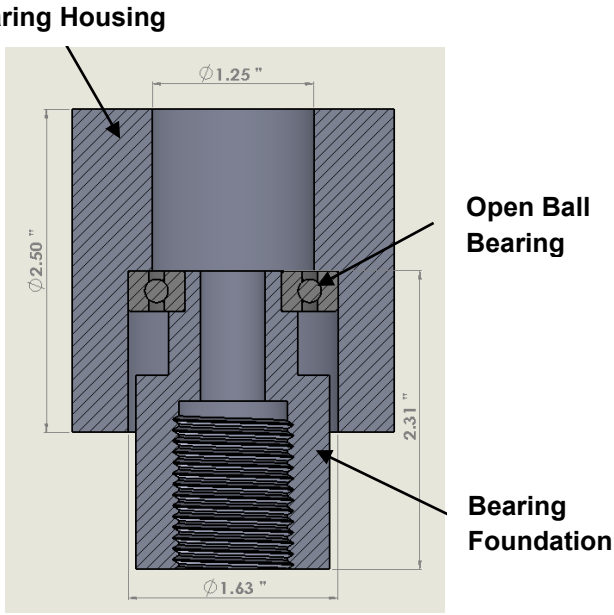

Figure 3.4: Passive yaw bearing assembly with basic dimensions (in).

Chapter 4: Electrical Design

4.1 Power Electronics

The power electronics system consists of four major components: a generator, an AC-DC converter, a DC-DC converter, and a load. Figure 5.1 illustrates the architecture of this system.

The generator produces 3-Phase AC voltage that needs to be rectified into DC voltage. A full-wave bridge rectifier was used to convert to a DC voltage and a capacitor was used to smooth it out. The rectifier utilizes VS-19TQ015-M3 Schottky diodes. These high-performance diodes have low forward voltage drops (0.32V) and have a reverse voltage limit that is tolerable (15V), making them suitable for this application.

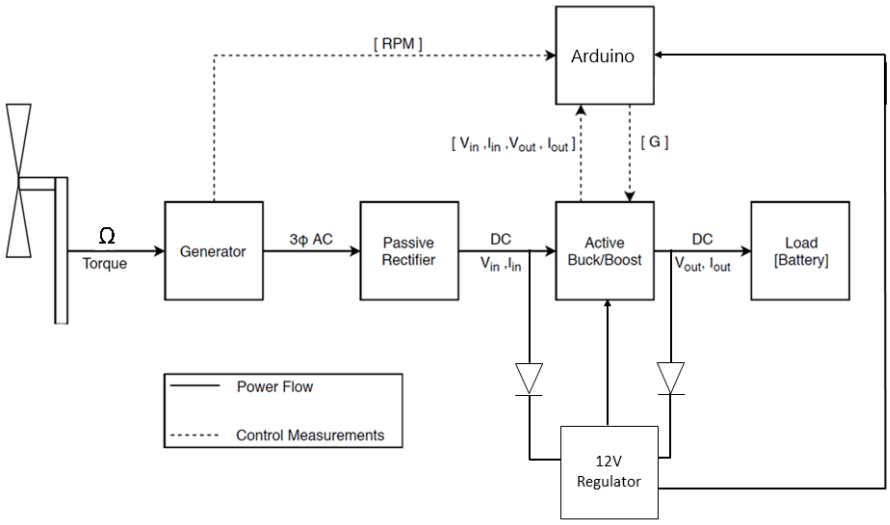

Figure 4.1: Power curve task flow diagram

The DC voltage output from the rectifier is regulated by a buck-boost (BB) converter. A buck-boost converter either steps down (buck) or steps up (boost) DC voltage. This is achieved by applying a gain of "G" to the input voltage where:

$$G = \frac{V_{out}}{V_{in}} \qquad \text{Equation 4.1}$$

The buck-boost converter decreases the voltage and increases the current in buck-mode and vice versa in boost-mode. The speed of the generator is roughly proportional to input voltage which can be controlled with the buck-boost converter. Due to our load selection, the output of the buck-boost

converter is roughly constant, thus a change in gain creates a change in input voltage, thereby controlling the speed. Controlling the speed of the generator allows for control of the power output at varying wind speeds. Without this control, the power output of the turbine would be not be optimized for a given wind speed. During operation, the gain of the converter can be adjusted so that the system is operating at its desired operating point.

Sizing of the capacitors and inductor in the converter was done using a Texas Instruments sizing document. The three parameters that needed to be considered were the input voltage (V_{in}), the output voltage (V_{out}), and the maximum output current (I_{outmax}). The maximum input voltage was taken from generator data and is assumed to be 15V. The output voltage is approximately 8V and the output current is approximately 6A. Taking these parameters into consideration, the inductor needs a minimum inductance of $40\mu H$ and the capacitor needs a minimum capacitance of $71\mu F$.

Lastly, the output of the converter reaches the load. This design utilizes a 6V lead-acid battery as the load – the objective of the system being to charge the battery. One of the biggest obstacles to overcome in the renewable energy industry is the storage of electricity. Using a battery as a load reflects one of the solutions used in the field. An additional benefit of using a battery as a load is that current can be drawn to power the control system prior to operation.

These circuits were initially prototyped using breadboards. Once their functionalities were confirmed, they were designed in EAGLE and printed into PCBs. An issue that we came across was high frequency noise caused by the current spikes in the MOSFETs. This noise was interfering with our instrumentation measurements. To remedy this, we grounded both the top and bottom plates of the buck-boost converter. Using this method in addition to proper grounding techniques, we were able to reduce the high frequency noise.

4.2 Theoretical System Performance

To model the operational characteristics of the electrical system relative to wind speed/power, a theoretical circuit was constructed. This theoretical circuit can be seen in the figure below:

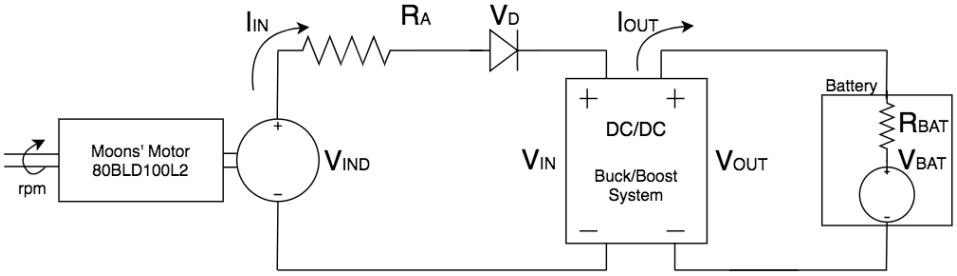

Figure 4.2: Theoretical system circuit

To consider the voltage drop across the diodes in the rectifier (3-Phase AC to DC conversion), V_D was added to the theoretical circuit. Similarly, to consider the armature resistance of the generator, R_A was added. Through benchtop tests, the values used in the system performance model were determined to be: $K_V = 0.00484\frac{V}{rpm}$, $V_D = 0.8V$, $\eta = 0.89$, $R_A = 0.4\Omega$, $R_{BAT} = 0.017\Omega$, and $V_{BAT} = 8V$. Using Figure 4.2, the theoretical circuit can be deconstructed into several equations. Solving these equations, the power generated by the wind turbine (P_{OUT}) can now be determined relative to system gain (G) and generator rpm (Ω). Similarly, using TSR and coefficient of power (C_P) information obtained from an analysis of our

blade design done in Qblade (Figure 2.3), we were able to determine the maximum obtainable power at various wind speeds—and what rotor speeds corresponded with the maximum power. The intersection of an aerodynamic wind power curve at a specified wind speed and an electrical power curve at a specified gain represent an operating point of the system. Below, both aerodynamic power delivered to the turbine (at various wind speeds), and electrical power generated (at various gain values), can be seen relative to rotor rpm (Ω) (Figure 4.3):

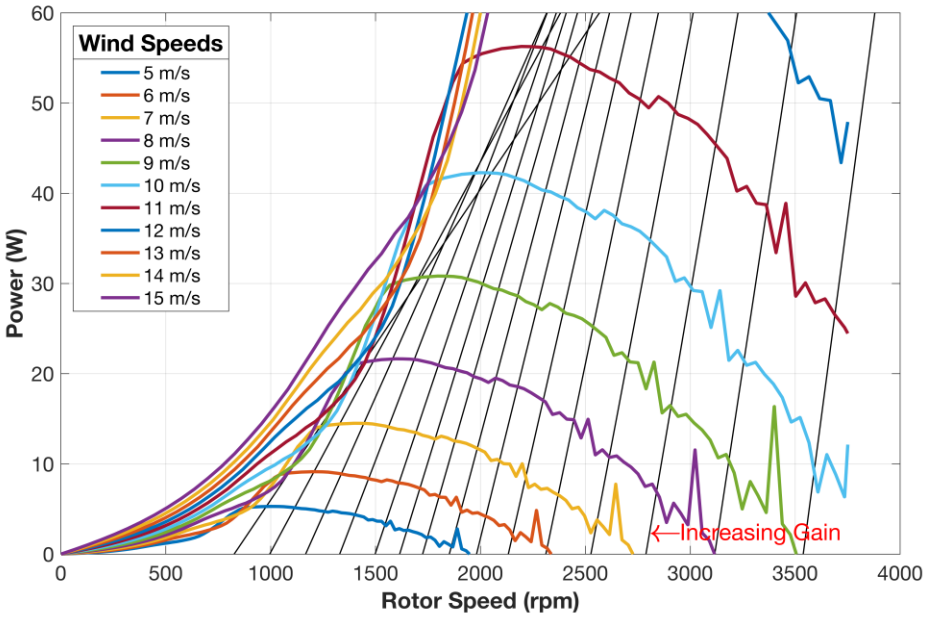

Figure 4.3: System power curves

To optimize power generated by the wind turbine, it is essential that the turbine operates near the peak of the wind power curve at a given wind speed. Above you can see the black lines represent power generated by our theoretical electrical system at various gain values (G). By adjusting gain in the control system, we were able to produce optimum power at varying wind speeds—allowing us to create a maximum power point control system. This maximum power point control system ensures that the system operates where the black lines intersect with the wind speed power curve peak. This ensures maximum power generation up to 11m/s.

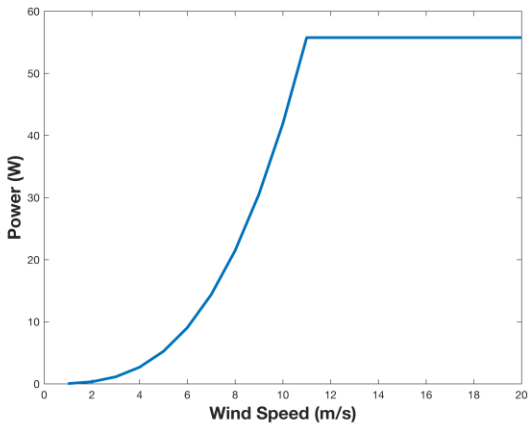

Figure 4.4: Theoretical power regulation curve

To accommodate competition guidelines, the maximum power point control system will plateau power production at wind speeds in excess of 11m/s. This power regulation is accomplished by utilizing the boost command previously discussed. This power regulation in relation to wind speed (not considering system losses) can be seen in Figure 4.4.

4.3 Electronic Speed Controller

The main electrical circuit comprising the electronic speed controller is a power inverter. The inverter is supplied with 6 VDC from the battery load and uses 6 MOSFETs, two for each phase, to convert the DC input to an AC output. The MOSFETS are operated by an Arduino signal that grounds a pull-up resistor by opening a transistor switch. During the operation of the inverter, only two MOSFETS are open at a time. One MOSFET connects one phase of the synchronous motor to the voltage supplied by the load, and the second MOSFET grounds one of the other two phases. This allows the direct current to flow through two phases of the motor creating the torque that spins the rotor.

A critical aspect of implementing the electronic speed controller in the turbine system is being able to switch from motor start-up, where power is being drawn from the load, to power generation. The switch between the two states is handled by a triple-pole double-throw electromechanical relay that is operated by an Arduino signal. The relay switches the three-phase output of the motor between the rectifier and the inverter and is connected so that it fails closed to the rectifier allowing for the minimum parasitic power loss when the turbine is attempting to produce power. During motor start-up, parasitic power losses are of little consequence. The implementation of the relay into the system is shown in Figure 4.5.

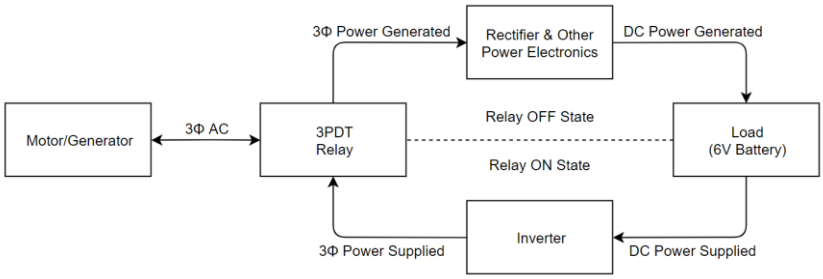

Figure 4.5: Motor start-up flow diagram

4.4 Durability Design

In addition to the main power electronic system, a second system was designed for the Durability Task. This second system can be seen in Figure 4.6. The main challenge of this task is to maintain a constant 5V output at the DOE provided variable resistive load for a variety of wind conditions. For some portions of the test, the wind will not be sufficient enough to maintain 5V at the load by itself, thus a 58F DOE provided supercapacitor must be used to provide the necessary energy.

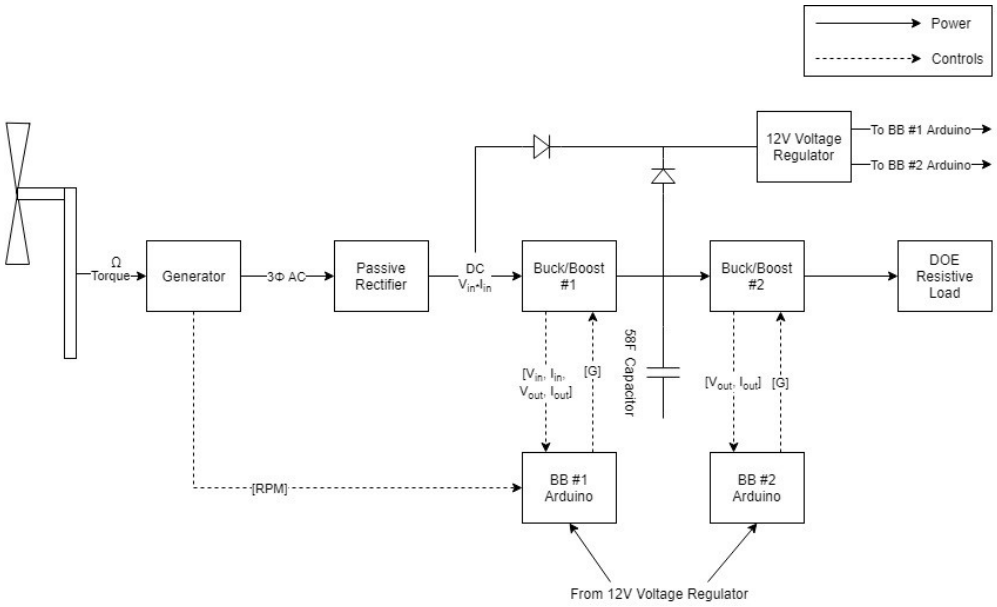

Figure 4.6: Durability task flow diagram

In this system, the AC power from the generator is first rectified to DC, and then put through a BB converter before going to the DOE provided supercapacitor. The main purpose of the BB converter is to optimally charge the supercapacitor via MPPT control code. While it is possible to charge the supercapacitor without this BB converter, this component is necessary to extract the maximum amount of power from the wind. The BB also applies a large initial buck in order to prevent the turbine from seeing 0V and slowing down as a result because the voltage the turbine sees is directly related to its rpm.

After the supercapacitor a second BB converter is placed before the power reaches the load. This second converter acts as a 5V voltage regulator and is controlled by a second Arduino microcontroller. The Arduino reads in current and voltage readings at the load via an INA219 current sensor, and then applies a gain via a proportional control code to the BB in order to maintain a constant 5V.

In order to supply the power needed to operate the BB converters and the Arduino which runs the control code, a diode assembly and off-the-shelf S18V20F12 12V voltage regulator were used. The diode assembly as seen in Figure 4.6. allows current to flow from the greater of two voltages: the turbine voltage or the capacitor voltage. This higher voltage current then passes through an off-the-shelf S18V20F12 12V voltage regulator. From the 12V regulator, power is drawn to the 20TQC45 MOSFET drivers and the Arduino. It might also be possible to use an off the shelf voltage regulator in place of the second Arduino, however our team was not successful in finding one that could handle currents up to 8A.

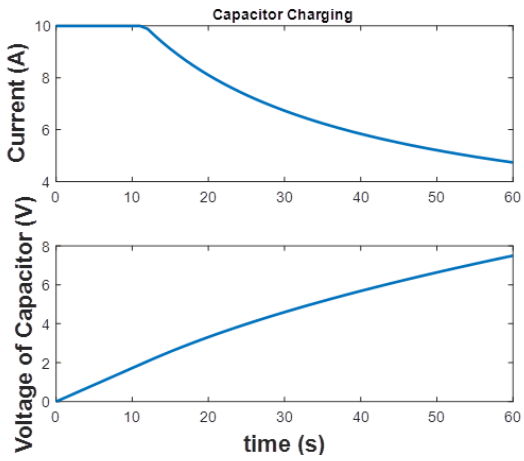

Figure 4.7: Capacitor charging numerical analysis

One key aspect in designing our Durability System was understanding the charging characteristics of the DOE provided supercapacitor. To this end, we numerically modeled an RC circuit with R = 0.2ohms (estimated resistance of wires plus the capacitor's internal resistance) and C = 58F, the capacity of the supercapacitor. We set the voltage source to output a constant 40W, the rated power of our turbine, in order to model the capacitor charging characteristics for the first minute. We also limited the capacitor voltage to 16V in the model. The numerical methods utilized iteratively solved a system of equations which include: Kirchhoff's Voltage Law, Ohm's Law, and the theoretical current flow through a capacitor. The numerical methods were calculated using MATLAB with the results shown in Figure 4.7.

Although the simulations do not completely depict the durability task in the first minute, they give us a better understanding of the supercapacitor's charging characteristics when given a constant power output which allowed us to better design the durability system.

4.5 LTspice Analysis

One of the main focuses of our engineering team this year was to rigorously analyze and refine our designs. For the electrical systems, this was done via transient simulations on LTspice in order to model the transient and steady-state behavior of our BB converters. LTspice is a computer software program which implements numerical methods in order to simulate the behavior of circuits. The LTspice schematic for the start-up/power curve task BB converter is shown in Figure 4.8.

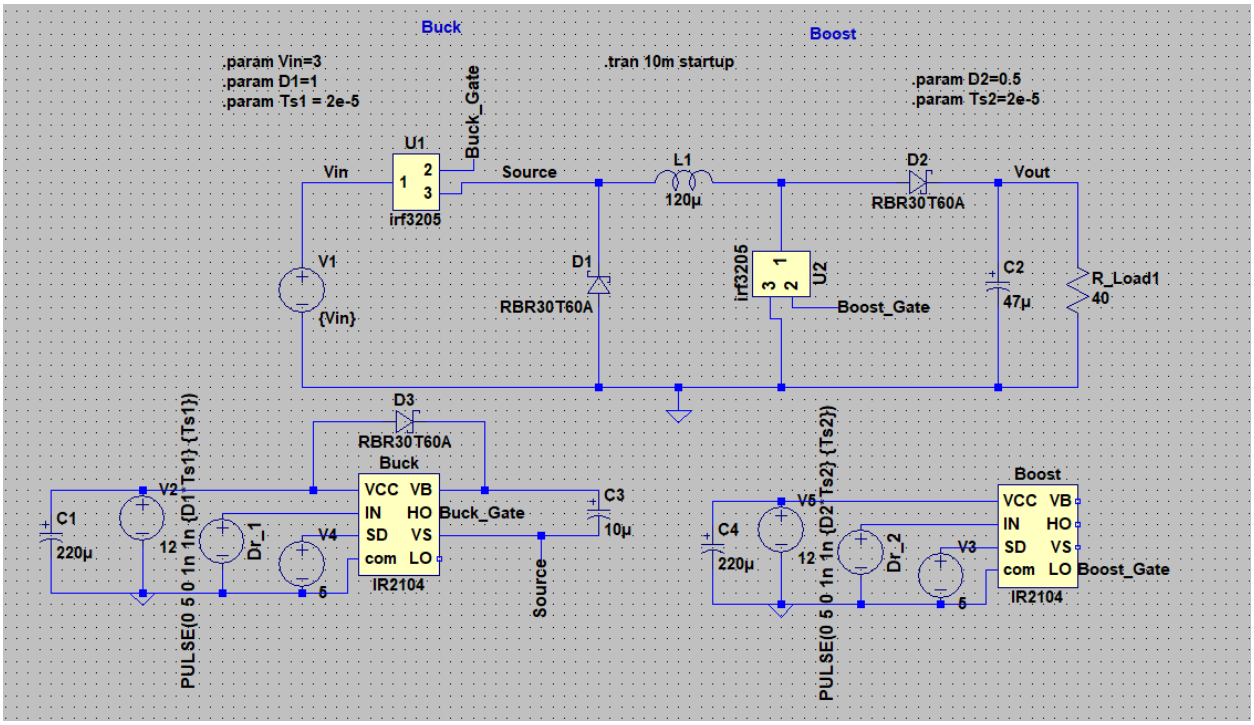

Figure 4.8: LTspice buck-boost schematic

The schematic in Figure 4.8 uses the exact drivers [9] and MOSFETS [10] in our physical BB converter. The SPICE files for these components were obtained directly from the manufacturer's websites. The transient and steady state response of the circuit in Figure 4.8 can be seen in Figure 4.9. We

compared the steady state response output voltage of the simulation to experimental measurements and found that the results match up quite nicely. We also compared the simulation's PWM and MOSFET gate voltage for a given operating condition with that of the physical model, taken via an oscilloscope. This can be seen in Figure 4.10 and Figure 4.11.

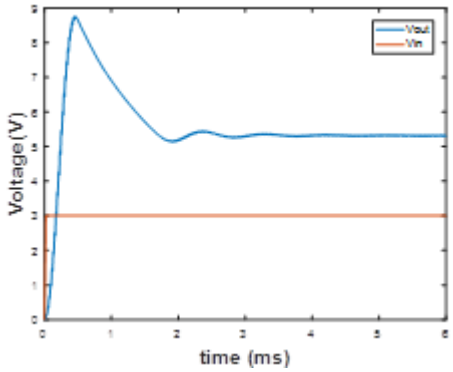

Figure 4.9: LTspice transient analysis

Figure 4.10: Experimental MOSFET gate and PWM wave forms

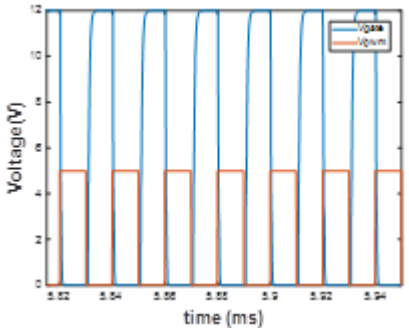

Figure 4.11: LTspice MOSFET gate and PWM wave forms

Verifying that the LTspice simulations were in agreement with our physical BB converter gave us confidence in our ability to use the simulations as a way of quickly prototyping different components and seeing the affects they have on performance.

Chapter 5: Control Software

5.1 Motor Speed Control

The timing of the inverter, which dictates what two MOSFETs should be opened at an instant in time, was determined using the position of the rotor given by three hall sensors built into the motor. The three hall sensors each having two states, high or low, creates six critical positions where the phases of the motor must be switched. The microcontroller reads the output of the hall sensors and uses a conditional statement to determine which MOSFETs to open to produce the highest amount of torque. Initially, the MOSFETs of the inverter that received power were switched after a constant set time. Using a constant switching time was unsuccessful as the inertia of the hub and blades prevented smooth rotation and starting at high speeds.

For greater control during motor start-up, it was decided to implement a function that controlled motor RPM. The RPM of the motor was controlled by using pulse width modulation on the Arduino signals that opened and closed the MOSFETs. The rapid switching of the MOSFETs caused by the PWM signal allowed for the voltage seen by the motor to be limited, effectively reducing motor speed. For superior control of motor speed, proportional control was implemented where the value for gain was determined experimentally. Integral and derivative control was also added to the function controlling RPM and were optimized through empirical tests. Ultimately, it was decided to remove the derivative control as it added extra complication to the RPM controlling function with little benefits.

5.2 Main Test

We compared and contrasted a variety of microcontrollers for the purposes of completing the Main Test and eventually decided on the Arduino MEGA2560. We chose to use an Arduino MEGA2560 due to its large amount of PWM pins, high resolution on timers, and large flash memory. We also chose the MEGA over non-Arduino boards with similar performances due to the engineering team having a good amount of familiarity with programming in the Arduino IDE as well as needing a guarantee of compatibility with Arduino libraries used in our sensors/timers. The code was made to switch between 5 different modes depending on the operating conditions of the turbine: Standby, Electronic Speed Control (ESC), Maximum Power Point Tracking (MPPT), Power Regulation, and Braking. A flowchart showing the switching conditions is shown in Figure 5.1.

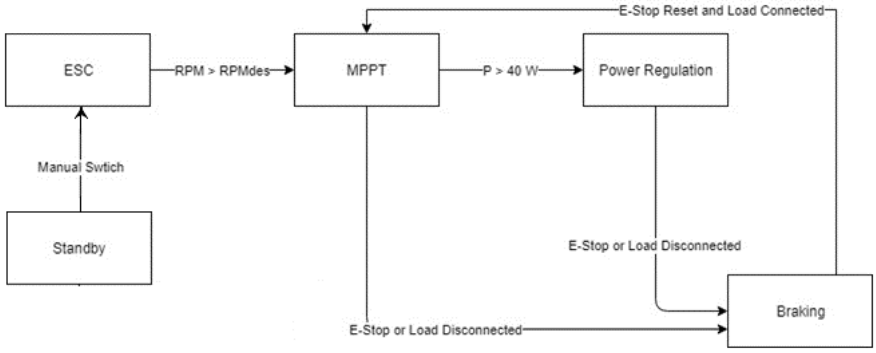

Figure 5.1: Main task state diagram

After the RPM is brought up to the desired value via the ESC, the turbine goes into MPPT mode. The goal of MPPT mode is to maximize the amount of power being produced for any given windspeed as long as that power is below the rated power of our turbine. This is done by using a control scheme based off of the System Power Curves in figure 5.3. We invert the graph and solve for the optimal RPM for a given power output, read via an INA219 sensor. The equation used is a cube root function (as wind power is a cubic function of wind speed, and at constant optimal TSR, the inverse is a cube root):

$$RPM_{opt} = a \times {P_{out}}^{b} \qquad \text{Equation 5.1}$$

Where α is an experimentally determined constant and b is (1/3). We determine α for each new testing location by solving for a new wind power curve for that location, and then plotting the data in excel. We then invert the resulting graph and curve fit a cube root function.

After calculating the optimal RPM, a new duty cycle for the buck boost converter is calculated via the following equation:

$$G_{new} = K_{MPPT} \times (RPM_{opt} - RPM) + G_{old} \quad \text{Equation 5.2}$$

This is a proportional control scheme where we multiply the difference between the actual and optimal RPM by some factor k and add the change to the old value of the duty cycle. This new duty cycle is then sent to the BB converter which will change the gain being applied to the voltage that the turbine sees. This will slow down or speed up the turbine to the optimal RPM due to Equation 3.1. Depending on the value of k, the rate at which the RPM of the turbine reaches the optimal RPM will change. Larger values cause faster convergence to the optimal RPM but with more oscillations, and smaller values cause slower convergence but with less oscillations about the optimal RPM.

When the output power read by the INA219 sensor exceeds the rated power of the turbine, the control scheme switches into power regulation mode. In this mode, a new duty cycle is calculated that will maintain the output power around the rated power. This is done in the following equation:

$$G_{new} = K_{RPC} \times (P_{out} - P_{rated}) + K_d \times (P_{out} - P_{old}) + G_{old} \quad \text{Equation 5.3}$$

Where K_{RPC} and K_d are experimentally determined constants which determine the speed of convergence and amount of oscillation about the rated power. This equation is a proportional – derivative control scheme where the difference between the actual and rated output power is added to the difference between the actual and old value of output power (multiplying both by some pre-factor). The derivative control serves to speed up the change in duty cycle if the difference between new and old power measurements is high, and at the case where $P_{out} = P_{old}$, the code simplifies to solely proportional control.

In order to make our system safe, we must be able to brake the turbine at any time when prompted or if the load is disconnected. The braking is accomplished by shorting the output of the generator with an electromechanical relay.

The INA219 current sensors used in our system use a low resistance, high accuracy, shunt resistor in order to determine current and voltage. The sensors use a precision amplifier with a voltage range of plus or minus 320mV in order to measure voltage across the resistor. Ohm's law can then be used to determine the current, as the resistor's value is known. The precision amplifier has an internal 12-bit ADC, thus by using a 0.033mΩ resistor, the sensor can read up to 9.697A with a resolution of 23.67mA.

5.3 Durability Test

For the durability test we use two different Arduinos, one for each BB converter. The first BB converter performs the same functions as the one in the Main Task (MPPT and Power Regulation), while the second BB converter acts as a 5V voltage regulator. The control code flow diagram for the Durability System can be seen in Figure 5.2.

The manner in which MPPT and Power Regulation is done for the first BB converter is the same as in the Main System. The difference is that an initial buck is applied to the first BB converter in order to prevent the turbine from seeing the zero voltage of the uncharged capacitor when the test starts. This results

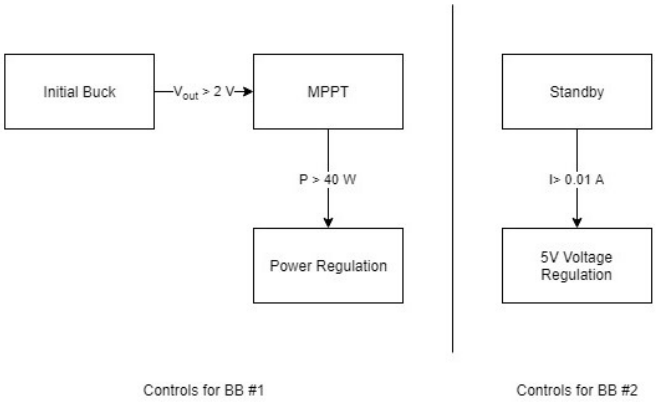

Figure 5.2: Durability task state diagram

in very low RPM and charging efficiency due to equation 3.1.

The second BB converter switches between two modes: Standby and 5V Voltage Regulation. The condition for switching is if non-negative current is detected by an INA219 sensor which is located just after the second BB converter. The voltage regulation is done via a simple proportional control scheme with a constant which is experimentally determined. As is the case in the other control codes, the value of the proportional constant determines the speed of convergence and amount of oscillation about the rated voltage of 5V.

Chapter 6: Testing

At California State University Maritime Academy, we have a custom built, open loop wind tunnel, which we used to conduct all our testing. The wind tunnel was constructed by the 2015–2016 California Maritime Academy's CWC team. The cross section of the wind tunnel's testing area is 3ft x 3ft, and is able to achieve wind speeds up to 14m/s. This is one constraint of our wind tunnel, as we are unable to use the wind tunnel to test the turbine at high wind speeds up to 20m/s. This prevents us from testing our electrical system and the structural integrity of the blades at high wind speeds.

We created our first iteration of the blades and the buck-boost converter which allowed us to conduct tests on our own turbine. During these tests, we examined the efficiency of the buck-boost converter, the start-up speed of the turbine, and created power curves for the blades by adjusting the gain of the buck-boost converter manually. Voltage and current measurements were taken from the output of the buck-boost converter and the power was then calculated. Using the power curves produced and the start-up data, we began an iterative process testing multiple blade designs. The final blade test data can be seen in Figure 6.1. Comparing these results with the theoretical results in Figure 4.4, it can be seen that we are actually producing about 47W at 11m/s, whereas the data from QBlade suggested that we should theoretically produce 53W. The data also shows that we could regulate the power output to the rated power at wind speeds above 11m/s. A start-up wind speed of 6.2m/s was found from testing, this is close to the QBlade analysis which calculated a start-up wind speed of 5.6m/s.

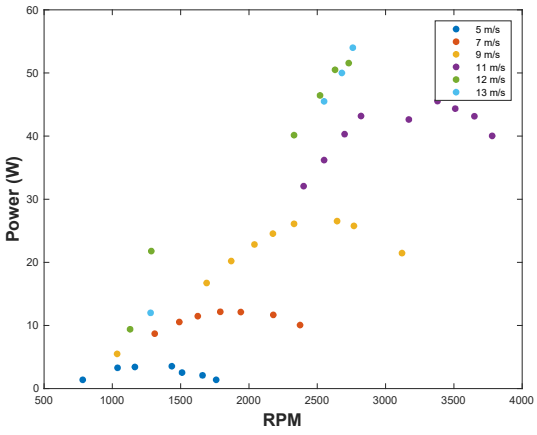

Figure 6.1: Experimental power curves

Testing played a critical role in ensuring the robustness of the electronic system. For start-up, we noticed during testing that the turbine RPM set from the ESC increased when subject to wind. Through testing we could determine how much the RPM increased at various wind speeds which gave us an approximate wind speed indication. We could then set an RPM tolerance for the inverter and have the relay trip when the turbine goes above that RPM. Using this technique, we were able to produce positive power around 4.7m/s which is earlier than the static cut-in wind speed of 6.2m/s. In addition, we found that the buck-boost converter had an efficiency range of 79-85% during MPPT operation. This is an improvement on linear voltage regulators and validates the choice of a switched-mode voltage regulator.

Bibliography

[1] *Electrical Engineering, Principals and Application*, 6th Edition by Allan R. Hambley, Pearson Prentice Hall

[2] Wood, D. (2011). Control Volume Analysis for Wind Turbines. *Small Wind Turbines Green Energy and Technology,*31-40. doi:10.1007/978-1-84996-175-2_2

[3] Manwell, J. F., McGowan, J. G., & Rogers, A. L. (2009). *Wind energy explained: Theory, design and application*. Chichester, U.K: Wiley.

[4] MIT. (n.d.). Area and Bending Inertia of Airfoil Sections. Retrieved from https://ocw.mit.edu/courses/aeronautics-and-astronautics/16-01-unified-engineering-i-ii-iii-iv-fall-2005-spring-2006/systems-labs-06/spl10b.pdf

[5] airfoiltools.com

[6] QBlade. (n.d.). Retrieved from http://www.q-blade.org

[7] Green, M. (2012, August). Understanding Buck-Boost Power Stages in Switch Mode Power Supplies (Rep. No. SLVA059A)

[8] Green, M. (2012, August). Design Calculations for Buck-Boost Converters (Rep. No. SLVA 535A)

[9] Infineon Technologies AG. "IR2104 Spice Model." *Infineon Technologies*, https://www.infineon.com/cms/en/product/power/gate-driver-ics/ir2104s/#!simulation.

[10] Infineon Technologies AG. "IRF3205 Spice Model." *Infineon Technologies*, www.infineon.com/cms/en/product/power/mosfet/20v-300v-n-channel-power-mosfet/40v-75v-n-channel-power-mosfet/irf3205/#!simulation.

[11] Young, Warren C, and Richard G Budynas. Roarks Formulas for Stress and Strain. McGraw-Hill, 2002.

[12] Craig, Roy R., and Timothy A. Philpot. Mechanics of Materials with MDSolids Software / by Timothy A. Philpot. Wiley, 2011.

[13] "Circle Segment Equations Formulas Geometry Calculator - Chord Length." Circle Segment Equations Formulas Geometry Calculator - Chord Length, www.ajdesigner.com/phpcircle/circle_segment_chord_c.php.